Proceedings of the 2022 IISE Annual Conference
K. Ellis, W. Ferrell, J. Knapp, eds.

Statistical and Spatio-temporal Data Features in Melt Pool Monitoring of Additive Manufacturing

Brandon Lane, Ho Yeung, Zhuo Yang
National Institute of Standards and Technology, Gaithersburg, MD, USA

Abstract

Co-axial melt pool monitoring is an in-situ method applied in laser-powder bed fusion additive manufacturing processes, which uses a high-speed camera optically aligned with the laser to continuously observe the melt pool. This results in a large volume of image data, which needs to be processed into data features that aim to be statistically correlated to processing or part quality metrics. One such processing method uses the laser position information to superimpose melt pool images onto the part coordinates, creating a stitched image or mosaic resembling part geometry. While superposition reduces the data volume and provides registration of melt pool image data to 3D part geometry, initial algorithms have so far demonstrated only a handful of static image features (e.g., maximum). This paper demonstrates an updated, generalized algorithm using dynamic arrays to efficiently store and process the image data. Using this generalized algorithm, multiple physics-based data features are demonstrated. Each feature is then discussed in terms of their physical relevance to fabrication quality, and potential for predictive process control.

Keywords
Laser powder bed fusion; melt pool monitoring; digital twin; superposition;

1. Introduction

Co-axial melt pool monitoring (MPM) is one of the more widely deployed in-situ monitoring methods for laser powder bed fusion (LPBF) additive manufacturing (AM) processes. In contrast to staring or off-axis imaging, co-axial MPM can enable much greater spatial resolution across the part surface by utilizing the laser-galvo system to ‘scan’ the camera field of view (*fov*) across the build plane in synchronization with the laser [1]. While data is acquired as an image stream, it is advantageous to register, visualize, and analyze MPM data within AM part coordinates. However, multiple algorithmic methods for this registration and visualization exist. Researchers at the National Institute of Standards and Technology (NIST) have recently focused on a method of co-axial MPM image ‘superposition’ [2]. Generally, this method takes sequential co-axial MPM images, registers to the corresponding laser spot position, and algorithmically combines overlapping images, thus converting a video stream into a high-resolution 2D static image, or mosaic, representative of each layer’s part geometry. Then, like the AM process, the layer-by-layer MPM-based mosaic images can be stacked into a virtual volume, or digital twin, of the printed part based on melt pool images.

Other researchers and commercial vendors have implemented the melt pool superposition concept. More often, MPM image superposition is demonstrated using staring-configuration imagers [3], [4], with a similar concept provided as a commercial monitoring product called ‘optical tomography’ (OT) [5]. However, this concept is more rarely tested on research-based co-axial MPM systems, but for a few examples [2], [6], and it is unknown yet by the authors if image superposition is used on similar commercial co-axial MPM imaging products [7].

The value of co-axial MPM and image superposition to construct 3D digital twins is clear. However, there is still great potential to explore 1) various types of superposition algorithms that may provide efficient or robust computation or storage of MPM superposition mosaic images, and 2) definition of additional, physics-informed MPM image features that target specific LPBF phenomena. This paper aims to explore and demonstrate both ideas, and build upon previous work at NIST [2].

2. Generalized Algorithm

The original algorithm for constructing the superimposed images is detailed in [2], and briefly reviewed. A machine coordinate system {A}, which coincides with the laser/galvo scan position on the build plane, is defined in units [mm]. The co-axial MPM image coordinates {M} are defined in units [pixel], or converted to units [mm] when multiplied by the instantaneous field of view (*ifov*, units [mm/pixel]). The MPM image {M} and machine {A} coordinate frame are co-oriented, while the {M} coordinate frame translates within {A} based on the laser scan positions in {A}. More details on these coordinate system definitions are defined in [8].

In the algorithm described in [2], each pair of successive MPM images, ${}^{M}p(x,y)$, is shifted in space with respect to the machine coordinates {A} by $(\vec{x}_i - \vec{x}_0)/ifov$, where $\vec{x}_i$ is the ${}^{A}(x,y)$ position of the laser spot for the i^{th} MPM image in units [mm]. The maximum value between any pixels from the two images spaced within {A} is stored in the 'mosaic image', ${}^{A}P(x,y)$, also defined in {A}. In the next iteration, the next MPM image frame is aligned and compared to the mosaic image, and once again the maximum pixel values retained. A schematic of the process shown in **Figure 1 left**. Although a 'max' operation was used in [2], any incremental operation (e.g., min, sum, count, etc.) acting between each subsequent MPM image and the accumulated mosaic image may be used. While algorithms exist for incremental mean, variance, etc., many statistical operations require access to the entirety of a sample set, and cannot be performed incrementally on new values. For this reason, and to enable more generalized computation among all superimposed pixels prior to formation of the MPM mosaic ${}^{A}P(x,y)$, overlapping pixels are retained in a grid of dynamic vectors, or 'cell array', as shown in **Figure 1 right**. Each cell or pixel in the array can vary in length. Since many of the pixel values in the MPM images are 0 or low, pixel values below a defined threshold are not stored in order to save memory. Once fully constructed, various kinds of operations may be applied to all retained values within each cell or pixel in the cell array.

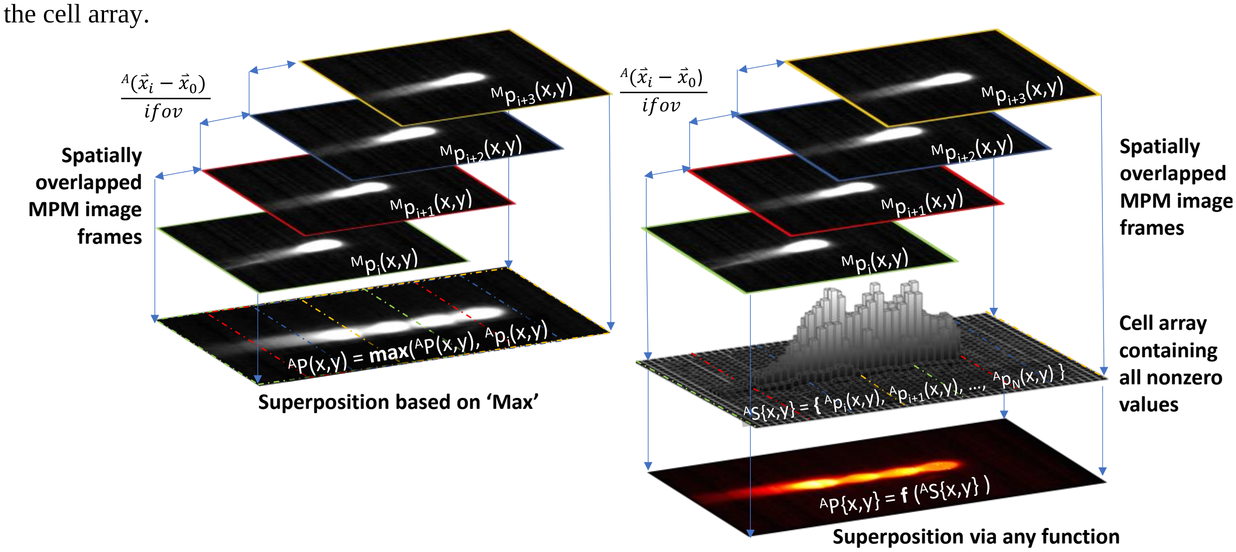

Figure 1: Example of original (**left**) and updated (**right**) algorithms for constructing superimposed MPM images. The original method calculated the maximum value of overlapping pixels. The updated algorithm accumulates pixel values within a cell array, then performs a functional operation on the entire population within each array.

In addition to accumulating pixel values, corresponding MPM image frame timing information (e.g., timepoint when each frame was acquired) may be simultaneously stored in a parallel and same-sized cell array. This enables further flexibility to compute temporal-based features. This generalized algorithm thus enables flexible calculation of myriad MPM superposition mosaic types based on statistical or physics-based concepts.

3. Example Dataset

For examples in this paper, we use the "OverhangPartX4" dataset acquired on the Additive Manufacturing Metrology Testbed (AMMT) at NIST [8]. This 3D build consists of four nominally identical parts fabricated from nickel alloy 625. Each part, as designed, is approximately 5 mm × 9 mm in footprint, and 5 mm tall with a 4 mm diameter cylindrical cutout, and 45° overhang, shown in **Figure 2**. The laser scan parameters used a nominally 195 W laser power and 800 mm/s scan speed, and a scan sequence that rotated 0° and 90° between even and odd layers, respectively.

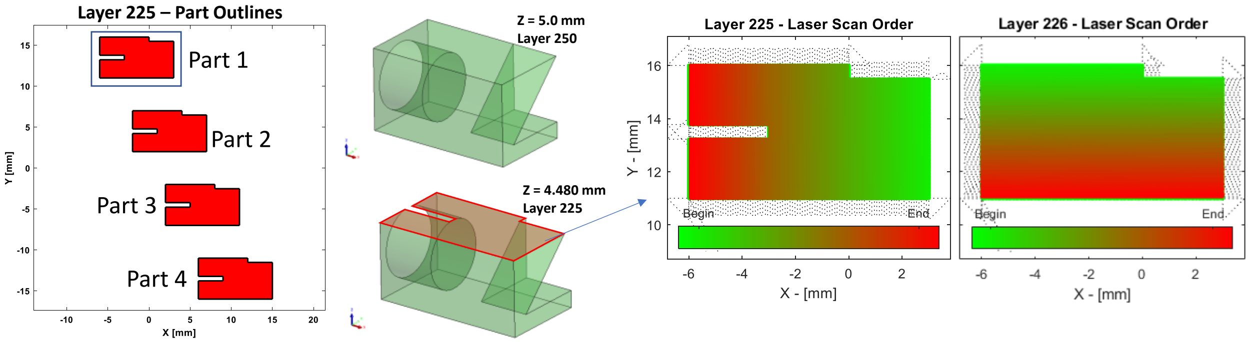

Figure 2: (**left**) Part locations and numbering, (**center**) design geometry of Part 1 including intermediate layers 225and 226 at the closure of the cylindrical feature, (**right**) laser scan sequence for two example layers. “Begin” (green) and “End” (red) mark the scan sequence.

The AMMT is controlled via ‘XYPT command’ files, as described in [2], [8]. These files consist of four columns of data, where each row is a 10 µs timestep (i.e., 100 kHz digital rate). The columns include X and Y scan positions in [mm], laser power P in [W], and MPM camera trigger column T. When the XYPT commands are executed on the AMMT, a nonzero value in the T column triggers the MPM camera to acquire an image, which can then be registered with the laser X and Y position in the corresponding columns. Co-axial MPM images were acquired on the AMMT at every 10 timesteps, with 20 µs integration time, (120 × 120) pixel image size, and 8-bit grayscale depth.

4. Statistical and Multi-variate Features

Figure 3 demonstrates superimposed MPM mosaics for three layers, where common statistical values are calculated for all overlapping pixel values. The standard error of the mean (SE) is also provided, which utilizes two combined metrics of standard deviation (σ) and number of nonzero pixels in each cell (n).

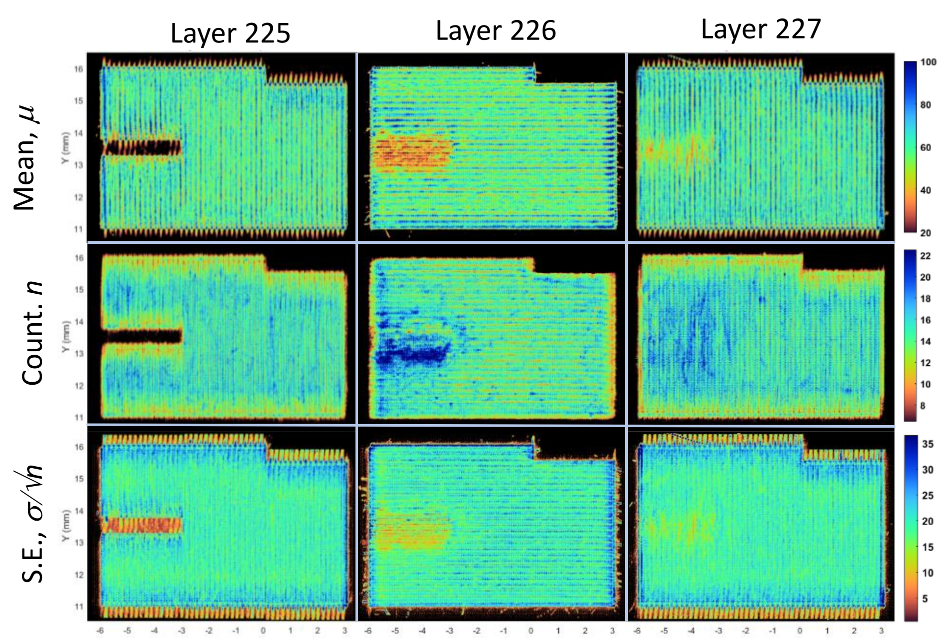

Figure 3: Example standard statistical features. Statistical operations are calculated for each overlapping pixel along the frame/time dimension.

5. Physics-based Features

To determine temperature-related metrics, the MPM camera was thermally-calibrated using a light-emitting-diode (LED) and integrating-sphere-based calibration source *in-situ* within the AMMT [9]. Calibration consisted of 13 measured temperature points, and the mean pixel values from the MPM images are compared to the reference temperatures of the calibration source, shown in **Figure 4 left**. A regression model was fit to the calibration points, resulting in parameters a = 906.2, b = 0.1546, and r^2 = 0.9998 for the power-law model $T_{rad} = aS^b$. T_{rad} is the radiance (e.g., blackbody-equivalent) temperature and S is mean pixel value in digital levels [DL]. Additionally, the effect of applying a hypothetical emissivity correction was tested by dividing S by $\epsilon = 0.5$. The temperature regression model was applied to MPM pixel-value cell arrays, then the mean cell temperatures calculated similar to **Figure 3**, resulting in the mean radiance and emissivity-corrected temperature mosaics in **Figure 4 right**. As can be expected, emissivity-corrected mean temperature values were generally higher than for radiance temperature. However, the mean temperature near the closure of the cylindrical feature appears lower, despite the expectation of greater accumulated heat due to reduced underlying solid structure to conduct heat from the melt pool [10]. Generally, MPM images in those regions show low temperatures for longer durations (i.e., more image frames), which influences the calculated mean value. Higher temperatures may exist for shorter durations but 1) these may diffuse relatively quickly and 2) are limited by camera saturation at equivalent $T_{rad} \approx 2000$ °C.

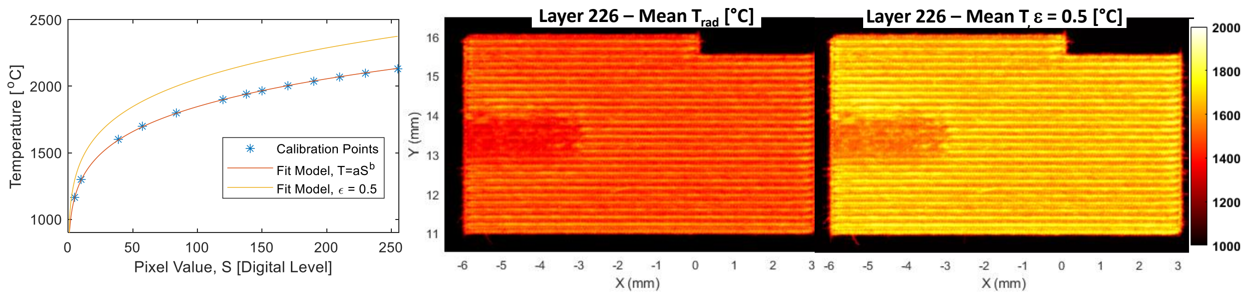

Figure 4: (Left) Example thermal calibration curve, and corresponding curve assuming emissivity $\epsilon = 0.5$. **(right)** Example mean radiance and emissivity-corrected temperature mosaics for Layer 226.

As mentioned in Sec. 2, frame numbering values are stored in a parallel cell array to the MPM pixel values, to be accessed for temporal calculations. Another feature called 'time above temperature' or 'time above threshold' has been demonstrated for staring camera systems [4], [11], [12], though it is unknown by the authors if it is yet demonstrated for co-axial MPM systems. The general algorithm requires signal or temperature data as a function of time for each pixel location, then counts the amount of time (i.e., number of image frames divided by frame rate) the temperature or signal is above a specified threshold level. **Figure 5** demonstrates 'time above temperature' for layer 226 at threshold values of 1800 °C and 1300 °C. Temperature vs. time data for three example pixels are also shown.

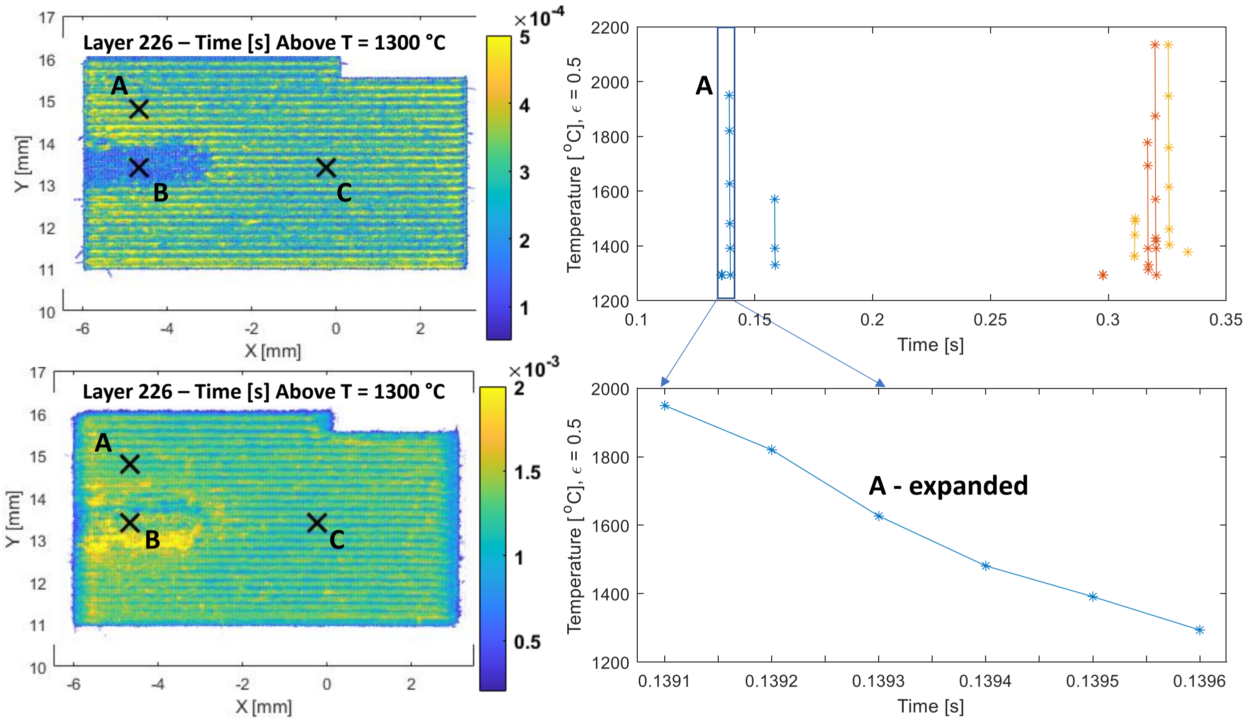

Figure 5: '**Time above temperature**' mosaic for layer 226 for 1800 °C (**top left**) and 1300 °C threshold values (**bottom left**). Corresponding temperature vs. time results are shown (**right**) for corresponding pixels A, B, and C shown in the left images.

Interestingly, the 'time above temperature' metric shows relatively lower values at the closure of the cylindrical feature (point B), compared to the rest of the part when utilizing a threshold temperature of 1800 °C. The opposite trend is shown when utilizing a temperature threshold of 1300 °C. This coincides with the prior observation and hypothesis for mean temperature: that lower temperatures are retained for longer time durations at the overhang.

6. Discussion

Several aspects still pose challenges to the co-axial MPM superposition concept. A frame rate that is too low or a scan speed too high may result in 'gaps' between superimposed melt pools, which is partially evident in the figures above. Due to the wide range of melt pool temperatures, MPM images are nearly all dark/zero in most pixels, and saturated near the melt pool center. Saturated pixel values are not directly related to melt pool radiant emission, and ought not to be utilized or considered in some calculations. Some melt pool phenomena such as spatter or plume may be visible in MPM image frames. These phenomena are normal, but may elicit some noise or perturbation to key metrics of interest such as melt pool size. Thus, some filtering or preprocessing of MPM images may be necessary, depending on the final mosaic type to be processed.

Ultimately, the co-axial MPM mosaic images demonstrated in this paper may be 'stacked' to form 3D volumes or digital twins of the AM parts, constructed solely of *in-situ* process monitoring data. Further work is necessary to create generalized algorithms for accumulating multiple layer data into a volume, and potentially enabling flexible operations applied between two or more adjacent layers. The generalized methods for single layers shown in this paper, however, are extendible to a multitude of different co-axial MPM image superposition functions.

References

[1] L. Mazzoleni, A. G. Demir, L. Caprio, M. Pacher, and B. Previtali, “Real-Time Observation of Melt Pool in Selective Laser Melting: Spatial, Temporal, and Wavelength Resolution Criteria,” *IEEE Trans. Instrum. Meas.*, vol. 69, no. 4, pp. 1179–1190, Apr. 2020, doi: 10.1109/TIM.2019.2912236.

[2] H. Yeung, Z. Yang, and L. Yan, “A Meltpool Prediction Based Scan Strategy for Powder Bed Fusion Additive Manufacturing,” *Addit. Manuf.*, p. 101383, Jun. 2020, doi: https://doi.org/10.1016/j.addma.2020.101383.

[3] J. A. Mitchell, T. A. Ivanoff, D. Dagel, J. D. Madison, and B. Jared, “Linking pyrometry to porosity in additively manufactured metals,” *Addit. Manuf.*, vol. 31, p. 100946, Jan. 2020, doi: 10.1016/j.addma.2019.100946.

[4] C. Lough, R. Landers, D. Bristow, J. Drallmeier, B. Brown, and E. Kinzel, “Experiment Based Superposition Thermal Modeling of Laser Powder Bed Fusion,” in *Proceedings of the Solid Freeform Fabrication Symposium*, Austin, TX, 2021, pp. 1326–1333.

[5] G. Zenzinger, J. Bamberg, A. Ladewig, T. Hess, B. Henkel, and W. Satzger, “Process Monitoring of Additive Manufacturing by Using Optical Tomography,” in *AIP Conference Proceedings*, Boise, ID, Mar. 2015, vol. 1650, pp. 164–170. doi: 10.1063/1.4914606.

[6] L. Zheng *et al.*, “Melt Pool Boundary Extraction and Its Width Prediction from Infrared Images in Selective Laser Melting,” *Mater. Des.*, vol. 183, p. 108110, Dec. 2019, doi: 10.1016/j.matdes.2019.108110.

[7] T. Kolb *et al.*, “Camera Signal Dependencies Within Coaxial Melt Pool Monitoring in Laser Powder Bed Fusion,” *Rapid Prototyp. J.*, vol. 26, no. 1, pp. 100–106, Jan. 2019, doi: 10.1108/RPJ-01-2019-0022.

[8] B. Lane and H. Yeung, “Process Monitoring Dataset from the Additive Manufacturing Metrology Testbed (AMMT): Overhang Part X4,” *J. Res. Natl. Inst. Stand. Technol.*, vol. 125, p. 125027, Sep. 2020, doi: 10.6028/jres.125.027.

[9] D. C. Deisenroth *et al.*, “Measurement Uncertainty of Surface Temperature Distributions for Laser Powder Bed Fusion Processes,” *J. Res. Natl. Inst. Stand. Technol.*, vol. 126, p. 126013, Aug. 2021, doi: 10.6028/jres.126.013.

[10] H. Yeung, B. Lane, and J. Fox, “Part geometry and conduction-based laser power control for powder bed fusion additive manufacturing,” *Addit. Manuf.*, vol. 30, p. 100844, Dec. 2019, doi: 10.1016/j.addma.2019.100844.

[11] G. Mohr *et al.*, “In-situ defect detection in laser powder bed fusion by using thermography and optical tomography—comparison to computed tomography,” *Metals*, vol. 10, no. 1, Jan. 2020, doi: 10.3390/met10010103.

[12] J. C. Heigel, B. M. Lane, and L. E. Levine, “In Situ Measurements of Melt-Pool Length and Cooling Rate During 3D Builds of the Metal AM-Bench Artifacts,” *Integrating Mater. Manuf. Innov.*, vol. 9, no. 1, pp. 31–53, Mar. 2020, doi: 10.1007/s40192-020-00170-8.